Three-Dimensional Study of the Vector Potential of Magnetic Structures

Charudatta Phatak and Amanda K. Petford-Long
Argonne National Laboratory, 9700 S. Cass Avenue, Argonne, Illinois 60439, USA

Marc De Graef*
Department of Materials Science and Engineering, Carnegie Mellon University, 5000 Forbes Avenue, Pittsburgh, Pennsylvania 15213, USA

(Received 20 February 2010; revised manuscript received 30 April 2010; published 21 June 2010)

The vector potential is central to a number of areas of condensed matter physics, such as superconductivity and magnetism. We have used a combination of electron wave phase reconstruction and electron tomographic reconstruction to experimentally measure and visualize the three-dimensional vector potential in and around a magnetic Permalloy structure. The method can probe the vector potential of the patterned structures with a resolution of about 13 nm. A transmission electron microscope operated in the Lorentz mode is used to record four tomographic tilt series. Measurements for a square Permalloy structure with an internal closure domain configuration are presented.

DOI: 10.1103/PhysRevLett.104.253901 PACS numbers: 75.75.Fk, 41.20.Gz, 81.70.Tx

Investigation of magnetic nanostructures for applications in various fields such as data storage, spintronic devices, magnetic logic devices, and magnetic random access memory [1,2], requires studying the physics underlying the magnetic interactions associated at such length scales. Also to correlate the properties with the structure, requires knowledge of the electromagnetic properties of the nanostructure, namely, the electrostatic and the vector potential rather than the associated fields [3]. The concept of the vector potential was introduced in electromagnetism around the middle of the 19th century [4]; Maxwell [5] proposed the name vector potential and a formal definition as the stored momentum per unit charge, similar to the electrostatic potential, which is the stored energy per unit charge. The vector potential $\mathbf{A}$ for a given magnetization $\mathbf{M}$ is given by the convolution of $\mathbf{M}$ with the dipolar kernel $\mathbf{r}/|\mathbf{r}|^3$. The vector potential is central to several areas of physics, such as superconductivity, the Aharonov-Bohm effect, quantum field theory and vacuum condensates [6–9]. However, a precise measurement and visualization of the vector potential of such structures in three dimensions has never been achieved. It should be noted that for a classical magnetostatic system, such as the one presented in this work, the vector potential is averaged over many atomic distances and is thus a *classical* vector potential, which means it cannot be used directly in quantum mechanical equations for studying spin motions in magnetic nanostructures. However, with recent advances in transmission electron microscopy (TEM), such as chromatic and spherical aberration correctors, it may become possible to measure the localized vector potential in such nanostructures in the near future.

Amongst the current techniques for probing the magnetic properties of nanostructures, such as TEM, scanning electron microscopy, and an array of scanning probe microscopies, TEM is widely used because of the high spatial resolution for the study of physical as well as magnetic structure. In TEM, the electromagnetic potentials of the nanostructures are studied using phase retrieval techniques such as electron holography [10] and the transport-of-intensity (TIE) technique [11]. These approaches rely on the concept of the Aharonov-Bohm effect [12], i.e., that the phase of the electron wave is modified due to the electromagnetic potentials of the nanostructure. A comprehensive theoretical background as well as experimental measurements of the phase shift due to the Aharonov-Bohm effect

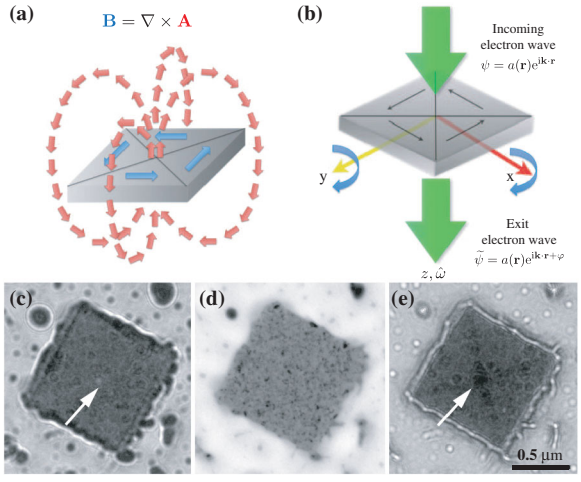

FIG. 1 (color). (a) The vector potential (red arrows) of a square particle with a closure magnetic domain configuration (magnetization is represented by blue arrows); black lines show the locations of 90° magnetic domain walls. (b) shows the basic setup of a VFET experiment in a TEM. Electrons travel along the direction of the green arrows, and experience a phase shift when they traverse the region around the magnetized thin foil (gray square prism). (c)–(e) show under-, in-, and over-focus Fresnel images of a square Py island. The vortex location is indicated with white arrows in both out-of-focus images.

are given by Peshkin and Tonomura [13]. Also, these methods usually result in two-dimensional (2-D) projections of the true three-dimensional (3D) structure. A combination of tomography and TEM has been applied to the study of the 3D structure and morphology of nanoparticles used as catalysts [14,15] as well as biological specimens [16]. In this Letter, we show that the combination of tomography with Lorentz TEM (LTEM) allows for the measurement and 3D reconstruction, with a high spatial resolution, of the vector potential of magnetic structures. We will present experimental data for a 1×1 μm square island consisting of a 27 nm thick layer of $Ni_{80}Fe_{20}$ alloy (Permalloy/Py). Figure 1(a) shows (in red) the schematic vector potential for a square structure with a central vortex. It should be noted that, while the magnetic structure forms a flux closure state with minimal stray fields, the vector potential is nonzero outside the sample and does not decay as rapidly as the field itself. In addition, the vector potential also has a strong out-of-plane component.

Vector field electron tomography (VFET) extends the concept of conventional tomography to the reconstruction of vector objects (e.g., velocity field, magnetic induction or vector potential). A single tomographic tilt series can be used to reconstruct only one component of a vector field; to reconstruct the second component, a second tilt series around a mutually orthogonal tilt axis is required. The basic setup for VFET in LTEM mode is shown in Fig. 1(b). The third component of the field can be obtained by making use of an external boundary condition. As stated before, this is a classical vector potential, so that it must vanish far away from its source [17]. This means that it must satisfy the Coulomb gauge condition $\nabla \cdot \mathbf{A} = 0$.

To reconstruct the vector potential by means of tomographic methods, we must establish first how the LTEM images provide information about the vector potential. As mentioned earlier, the phase shift due to the electrostatic and vector potentials can be written as a sum of two terms (SI units), $\varphi(\mathbf{r}_\perp) = \varphi_e(\mathbf{r}_\perp) + \varphi_m(\mathbf{r}_\perp)$, where

$$\varphi_e(\mathbf{r}_\perp) = \frac{\pi}{E\lambda} \int_{-\infty}^{+\infty} V(\mathbf{r}_\perp + \ell\mathbf{e}) d\ell \tag{1}$$

is the electrostatic phase shift and

$$\varphi_m(\mathbf{r}_\perp) = -\frac{e}{\hbar} \int_{-\infty}^{+\infty} \mathbf{A}(\mathbf{r}_\perp + \ell\mathbf{e}) \cdot \mathbf{e} d\ell \tag{2}$$

is the magnetic phase shift; E is the relativistic electron accelerating potential and λ the wavelength. The integration is performed along the electron propagation direction $\mathbf{e}$ and $\mathbf{r}_\perp$ is a position vector in a plane normal to $\mathbf{e}$. In the tomography literature, $\varphi_e(\mathbf{r}_\perp)$ is known as the scalar x-ray transform of the potential $V(\mathbf{r})$, and $\varphi_m(\mathbf{r}_\perp)$ is known as the vectorial x-ray transform of $\mathbf{A}(\mathbf{r})$. Reconstructing $\mathbf{A}$, therefore, requires measurement of $\varphi_m(\mathbf{r}_\perp)$. The Fresnel (out-of-focus) imaging mode is used to recover quantitatively the total phase shift of the electron wave by means of the TIE technique [18]. In this work, we have employed a Fourier transform method to solve the TIE and recover the phase shift [19]. The magnetic phase shift can be extracted from the total phase shift using time reversal symmetry, which is implemented by flipping the sample upside down inside the electron microscope. The magnetic phase shift can then be obtained as the difference of the reconstructed phases for the sample in regular and upside down orientations. Lade *et al.* [20] first described the application of tomography to the reconstruction of various electromagnetic quantities. Tomographic filtered back-projection equations applicable to LTEM with particular focus on phase reconstruction using the TIE technique can be found in [21].

A 27 nm Permalloy (Py) thin film was deposited by magnetron sputtering on a square TEM grid with a SiO support membrane. Squares and ellipses were then patterned in the film using focused ion beam (FIB) milling. The grids were mounted in a tomography holder and loaded into a JEOL 2100F TEM operated at 200 kV and equipped with a special low field pole piece for magnetic characterization. Two tilt series about orthogonal axes were recorded (tilt range $\pm 70°$, $2°$ tilt increment); a three-image through-focus series was acquired for each tilt angle. This was followed by a sample flip of $180°$ and two more tilt series were acquired under identical conditions. The magnetic phase shift was then extracted from pairs of reconstructed phase maps and used for the reconstruction of the vector potential, $\mathbf{A}$. Figures 1(c)–1(e) show the under-, in-, and over-focus Fresnel images of the square island in the zero-tilt orientation. From these images, we derive that the magnetic structure of the square consists of a single vortex with $90°$ domain walls, leading to an overall closure domain configuration.

Figure 2(a) shows a schematic of the square island; (b) shows a line profile of the theoretical (continuous) and reconstructed (dotted) A_z component along the line AB indicated in (a). Figure 2(c) shows gray-scale plots of the theoretical (upper row) A_z component of the vector potential, computed using LLG micromagnetic simulations [22], and the experimentally reconstructed A_z component (bottom row). It should be noted that both magnitude and shape of the reconstruction are in good agreement with theoretical expectations, except near the edges of the patterned structure. Deviations near the edge of the field of view are due to the limited tilt range leading to a missing wedge of information. The reconstruction was performed on a 256^3 grid with a voxel size of 6.52 nm.

Inspection of the reconstructed vector potential shows that the sign of A_z relates to the chirality of the vortex state. From the line profile in Fig. 2(b), it can be seen that A_z is positive near the center of the island, where the vortex is located, decreases towards the edges, and changes sign just outside the island. This result demonstrates the capability of the VFET technique to reconstruct quantitatively, with high spatial resolution, the 3D vector potential of a square Py structure.

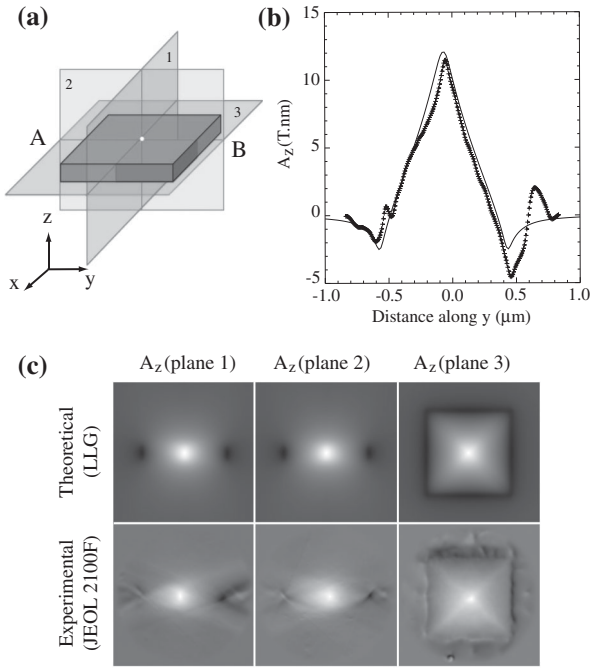

FIG. 2. (a) Schematic of the square island and coordinate axes; (b) line profile along the line AB of (a) of the theoretical (solid line) and reconstructed (crosses) A_z component of the vector potential; (c) gray-scale plots of the theoretical (upper row) and reconstructed (bottom row) A_z component of the vector potential along the planes indicated in (a).

Figure 3 shows the $B_x(0, y, 0)$ and $B_y(x, 0, 0)$ profiles computed from the experimentally reconstructed vector potential by a finite difference implementation of the relation: $\mathbf{B} = \nabla \times \mathbf{A}$. The magnitude of the reconstructed induction agrees well with the predictions from micromagnetic simulations. There are some deviations near the edges of the island, presumably due to Fresnel fringes in the out-of-focus images. This example shows that it is possible to compute magnetic quantities starting from the reconstructed vector potential, and obtain reasonable agreement with numerical/theoretical results.

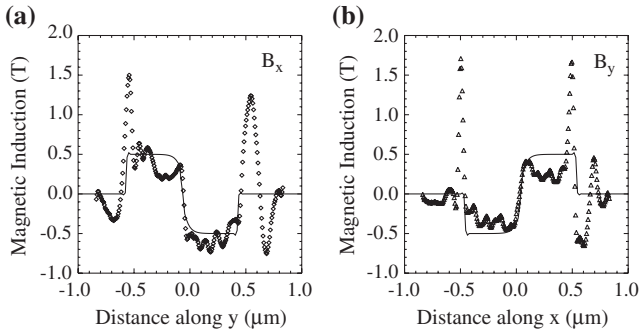

FIG. 3. Line profiles of the theoretical solid line) and reconstructed (symbols) $B_x(0, y, 0)$ (a) and $B_y(x, 0, 0)$ (b) components of the magnetic induction.

The agreement between the theoretical and reconstructed vector potentials is not perfect, and the largest deviations are found near the edges of the structure. There are two major reasons for these deviations: (i) the tomographic tilt series were recorded only in the tilt range $\pm 70°$, which results in an angular wedge of missing information. This introduces reconstruction errors, such as elongations and blurring, which are particularly noticeable in section planes 1 and 2 of Fig. 2(c); (ii) since the phase recovery method is an out-of-focus method, there is some loss of spatial resolution due to defocus blurring. In addition, the large defocus values used to acquire the images cause Fresnel interference fringes to appear near the edges of the structures, which, in turn, introduces local errors in the reconstructed phase. When two reconstructed phases are subtracted from each other to recover the magnetic phase shift, slight misalignments introduce errors in the phase separation; these errors then propagate to the 3D reconstructions. The effects of the missing wedge and the microscope defocus are seen clearly by comparing the two rows of Fig. 2(c). We anticipate that the reconstructions will benefit from the implementation of an iterative reconstruction method, similar to the one described by Arslan, Tong, and Midgley [23].

Figure 4(a) shows a 3D visualization of the magnetic induction near the x-y plane of the square island, clearly revealing the vortex configuration and the 90° domains. Figure 4(b) shows the 3D vector potential for the square

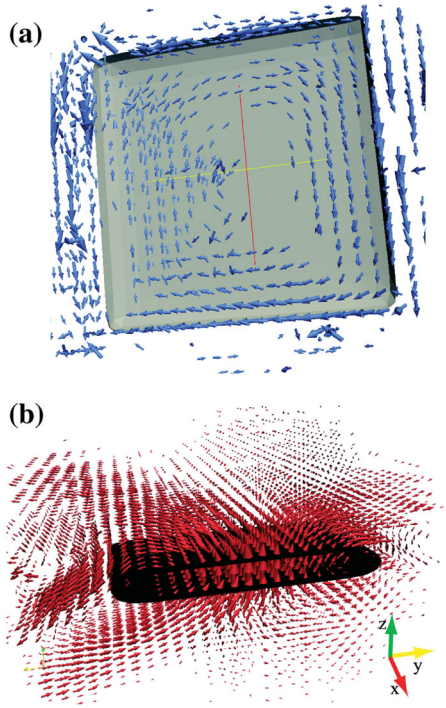

FIG. 4 (color). 3D visualization of all the physical quantities that can be recovered from a single VFET experiment, namely, (a) the 3D magnetic induction, and (b) the 3D vector potential. The gray outline in (a) and (b) indicates the shape of the square island.

island; the red arrows indicate the local direction of the vector field. The vector potential has a large z component at the vortex core and gradually decreases towards the edge and reverses direction just outside the edge of the island. The rotational character of the vector potential is clearly observed in this oblique view.

We have shown in this contribution that the combination of phase-reconstructed Lorentz microscopy and tomographic reconstruction allows for the quantitative 3D determination of the vector potential, $\mathbf{A}(\mathbf{r})$, of a micron-sized planar Permalloy element. From the phase reconstructions, one can derive both the electrostatic potential, which provides information about the shape of the element, and the vector potential, with a spatial resolution of a few nanometers. The technique described in this Letter will benefit from the use of aberration corrected electron microscopes, which will permit better quality phase reconstructions and, thus, better tomographic reconstructions. We anticipate that this approach will be used in the near future to gain an understanding of the vector potential and its implications, particularly in areas of magnetism and superconductivity. From the measured vector potential, the magnetic field distributions in and around particles with dimensions in the submicron range can be simultaneously derived along with their shape, which will be particularly useful to elucidate magnetostatic interactions between neighboring elements in patterned magnetic arrays. We have applied the VFET approach to other shapes, such as elliptical islands, as well as MFM tip and Co nanoparticle agglomerates. In a recent review article [24], Midgley and Dunin-Borkowski discuss various applications of tomography to materials science and life sciences, including 3D reconstructions of complex catalysts and precipitates, magnetotactic bacteria containing magnetite crystals, and symmetrical p-n junctions. The technique demonstrated in the present paper expands the arsenal of TEM-based characterization tools to include three-dimensional magnetic characterization. This technique not only provides information about the magnetic state of the sample, but the recovered electrostatic phase shift contains information about local variations of the electrostatic potential in the sample, which, in turn, leads to characterization of 3D charge densities. The combination of reconstructed electromagnetic potentials with the high spatial and chemical resolution of other TEM-based observation modes will be a tremendous aid to the design and fabrication of advanced devices and sensors.

We would like to thank M. Tanase for help with sample preparation and A. Imre for help with FIB patterning. The CMU portion of this work was supported by the U. S. Department of Energy, Basic Energy Sciences under contract DE-FG02-01ER45893. Some of this work was carried out at Argonne National Laboratory, a U. S. Department of Energy Office of Science Laboratory operated under contract DE-AC02-06CH11357 by University of Chicago Argonne, LLC. We also acknowledge use of the Center for Nanoscale Materials at Argonne National Laboratory (contract DE-AC02-06CH11357).

*degraef@cmu.edu; URL: http://materials.cmu.edu/degraef

[1] D. A. Allwood, G. Xiong, C. C. Faulkner, D. Atkinson, D. Petit, and R. P. Cowburn, Science **309**, 1688 (2005).
[2] S. A. Wolf, D. D. Awschalom, R. A. Buhrman, J. M. Daughton, S. von Molnar, M. L. Roukes, A. Y. Chtchelkanova, and D. M. Treger, Science **294**, 1488 (2001).
[3] E. J. Konopinski, Am. J. Phys. **46**, 499 (1978).
[4] E. T. Whittaker, *A History of the Theories of Aether and Electricity from the Age of Descartes to the Close of the Nineteenth Century* (Longmans, Green, London, 1910).
[5] J. C. Maxwell, *A Treatise on Electricity and Magnetism* (Dover Publications, New York, 1954), unabridged 3rd ed.
[6] F. V. Gubarev, L. Stodolsky, and V. I. Zakharov, Phys. Rev. Lett. **86**, 2220 (2001).
[7] M. D. Semon and J. R. Taylor, Am. J. Phys. **64**, 1361 (1996).
[8] R. C. Jaklevic, J. J. Lambe, A. H. Silver, and J. E. Mercereau, Phys. Rev. Lett. **12**, 274 (1964).
[9] R. G. Chambers, Phys. Rev. Lett. **5**, 3 (1960).
[10] E. Snoeck, C. Gatel, L. M. Lacroix, T. Blon, S. Lachaize, J. Carrey, M. Respaud, and B. Chaudret, Nano Lett. **8**, 4293 (2008).
[11] T. C. Petersen, V. J. Keast, and D. M. Paganin, Ultramicroscopy **108**, 805 (2008).
[12] Y. Aharonov and D. Bohm, Phys. Rev. **115**, 485 (1959).
[13] M. Peshkin and A. Tonomura, *The Aharonov-Bohm Effect*Lecture Notes in Physics (Springer, Berlin, 1989), Vol. 340.
[14] O. Abrosimov, E. Moroz, and A. Chuvilin, Kinet. Catal. **47**, 464 (2006).
[15] M. Weyland, Top. Catal. **21**, 175 (2002).
[16] D. J. De Rosier and A. Klug, Nature (London) **217**, 130 (1968).
[17] G. Rousseaux, Europhys. Lett. **71**, 15 (2005).
[18] D. Paganin and K. Nugent, Phys. Rev. Lett. **80**, 2586 (1998).
[19] V. V. Volkov, Y. Zhu, and M. De Graef, Micron **33**, 411 (2002).
[20] S. J. Lade, D. Paganin, and M. J. Morgan, Opt. Commun. **253**, 392 (2005).
[21] C. Phatak, M. Beleggia, and M. De Graef, Ultramicroscopy **108**, 503 (2008).
[22] M. R. Scheinfein, LLG Micromagnetics Simulator, 2009, 2nd ed., http://llgmicro.home.mindspring.com/.
[23] I. Arslan, J. R. Tong, and P. A. Midgley, Ultramicroscopy **106**, 994 (2006).
[24] P. A. Midgley and R. E. Dunin-Borkowski, Nature Mater. **8**, 271 (2009).